# A Novel Topology for Solar PV Inverter Based on an LLC Resonant Converter With Optimal Frequency and Phase-Shift Control

Necmi Altin , Senior Member, IEEE, Saban Ozdemir, Senior Member, IEEE, Mehdy Khayamy, Member, IEEE, and Adel Nasiri, Fellow, IEEE

Abstract-In this article, a new topology for a grid-connected solar photovoltaic inverter for the direct connection to the mediumvoltage grid is proposed. This topology employs an LLC resonant converter with a high-frequency (HF) isolation transformer in the dc-dc stage. The output of the dc-dc stage is a rectified sine wave voltage and current at the line frequency. An unfolder inverter interfaces between this dc stage and the grid. A combined phase-shift and frequency control method is used to control the LLC resonant converter. The phase-shift angle and switching frequency values of the LLC resonant converter are regulated to track the reference current signal for the whole operation range. The Lagrange multiplier method is applied to find the optimal trajectory to calculate the optimal phase-shift angle and switching frequency pairs for any operation condition by considering power converter and HF transformer losses to achieve the highest efficiency at a varying current. The transformer leakage and magnetization inductances are properly designed to provide a zero-voltage switching (ZVS) for a wide operation area, and additional resonant inductor requirement is removed. The LLC converter operates in a ZVS region except in a narrow band around the zero-current crossings of the inverter output. Using an HF transformer in the LLC resonant converter, a bulky line frequency transformer requirement is eliminated, and thus, a more compact and efficient design is obtained. The proposed topology is validated by the simulation and experimental results.

Index Terms—Combined modulation, Lagrange multiplier, LLC resonant converter, medium voltage (MV), solar inverter.

## I. INTRODUCTION

N THE last three decades, many studies have been performed on inverters used for renewable energy applications [1]. In

Manuscript received July 27, 2021; revised October 31, 2021 and January 19, 2022; accepted March 13, 2022. Date of publication March 29, 2022; date of current version July 19, 2022. Paper 2021-SECSC-0694.R2, presented at the 2019 IEEE Energy Conversion Congress and Exposition (ECCE), Baltimore, MD USA, Sep. 29–Oct. 3, and approved for publication in the IEEE TRANSACTIONS ON INDUSTRY APPLICATIONS by the Renewable and Sustainable Energy Conversion Systems Committee of the IEEE Industry Applications Society. This work was supported by the National Science Foundation under Grant 1650470. The work of N. Altin and S. Ozdemir was supported by the Scientific and Technological Research Council of Turkey (TUBITAK) BIDEB-2219 Postdoctoral Research program. (Corresponding author: Adel Nasiri.)

Necmi Altin and Saban Ozdemir are with the Department of Electrical and Electronics Engineering, Faculty of Technology, Gazi University, 06560 Ankara, Turkey (e-mail: naltin@gazi.edu.tr; sabanozdemir@gazi.edu.tr).

Mehdy Khayamy is with the Motiv PS, Hayward, CA 94545 USA (e-mail: mkhayamy@uwm.edu).

Adel Nasiri is with the Electrical Engineering Department, University of South Carolina, Columbia, SC 29208 USA (e-mail: nasiri@uwm.edu).

Color versions of one or more figures in this article are available at https://doi.org/10.1109/TIA.2022.3163372.

Digital Object Identifier 10.1109/TIA.2022.3163372

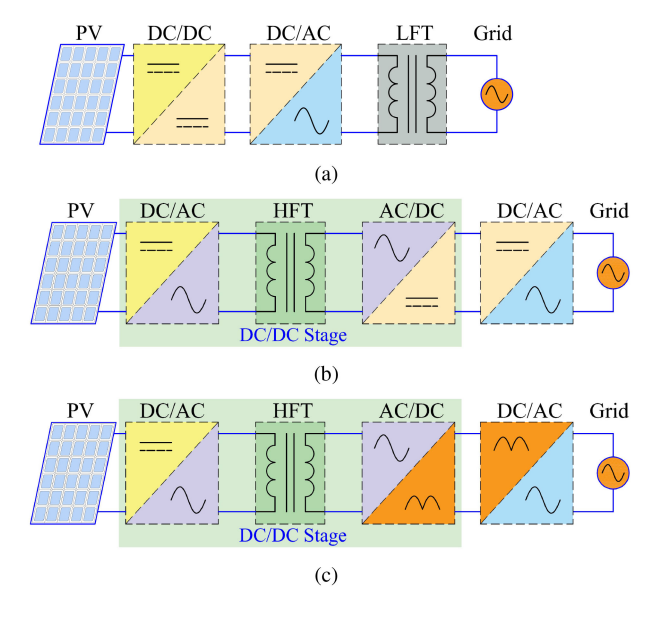


Fig. 1. Grid-connected inverters: (a) with LFT, (b) with HFT, and (c) proposed system.

most cases, line frequency transformers (LFTs) have been used at the output of the inverters to provide galvanic isolation and voltage matching as shown in Fig. 1(a). These transformers are also essential equipment for medium-voltage (MV) penetration of high power renewable energy plants. However, these transformers increase the cost, weight, and size of the system and decrease the efficiency. Generally, the transformer core loss exists even if the inverter is not exporting the power. Therefore, high-frequency transformers (HFTs) embedded in the dc-dc converters or dc-ac inverters have been proposed instead of the LFTs, as illustrated in Fig. 1(b). This topology is also called high-frequency-link inverter. While the HFT used in this topology provides same advantages as the LFT, it decreases the size and weight, and improves the efficiency due to much lower loss. This topology has been used for mostly low power applications. A high-voltage and frequency switching requirement for the second stage (grid side) inverter limits its applicability for high power and MV systems. To remove this drawback, the control of the dc-dc converter can be modified to generate the rectified sine wave voltage and current at the dc bus as shown in Fig. 1(c).

0093-9994 © 2022 IEEE. Personal use is permitted, but republication/redistribution requires IEEE permission. See https://www.ieee.org/publications/rights/index.html for more information.

Then, the dc–ac inverter stage works as an unfolder circuit and operates at the line frequency [2]–[5].

Different modular and multilevel inverter topologies have been investigated for the MV grid penetration of high power renewable energy systems considering the voltage and current limitations of the semiconductor switches [6]. Although, these topologies can improve the system reliability by replacing electrolytic capacitors with film capacitors, due to employing high-frequency isolated dc-dc converters, higher number of switches limits this improvement and affects the efficiency of the system. Furthermore, needs for additional balancing circuits and more complicated control schemes increase the complexity of the converter. Recent advancements in wide-bandgap semiconductor devices, especially silicon carbide (SiC) devices, allow direct connection of single-stage converters to the MV grid and can make the converter topology simpler [3]. However, cost of these switches and drive circuits are still too high for most applications.

Isolated unidirectional or bidirectional dc-dc converters have been commonly used and investigated for high-frequency-link inverter topologies. Dual-active bridge (DAB) converters have become a popular technology offering a higher power capability, lower filter requirement, and ease of realizing soft-switching features [7], [8]. The direction and amount of the power can easily be controlled by controlling the phase shift between the primary and secondary ports. However, this method can result in a higher circulating current and a narrow zero-voltage-switching (ZVS) region. Different modulation schemes such as the trapezoidal and triangular modulation have been proposed to overcome these problems. However, a single method cannot fully remove all the problems. The combinational use of these modulation schemes can provide a better performance with the expense of high control complexity with many parameters. Optimization of these parameters is another complicated process for these combinational methods [9].

The *LLC* resonant converters have been designed and used for various applications from a few watts to tens of kilowatts with their natural ZVS, zero-current-switching (ZCS), and buck or boost mode operation capabilities [10]–[13]. The *LLC* resonant converter provides ZVS at turn ON for primary-side switches. Turn-OFF loss is independent from the load, and therefore, it can be kept low. In addition, the circulating current of this converter can be controlled by the proper design of the magnetizing inductor of the transformer. The output voltage of the LLC resonant converter is a function of the switching frequency. Therefore, the frequency modulation is commonly used for these converters [14]. The phase-shift control is another control strategy applied to the *LLC* resonant converters. In this method, a phase shift is applied between the full-bridge inverter legs, and thus, a gain, independent from the switching frequency, is obtained. This gain can be controlled between 0 and 1 with the phase-shift angle. This enables limiting the maximum switching frequency and provides a wider range to select optimal magnetizing inductance to reduce the circulating current and improve the efficiency. In the literature, the phase-shift modulation method is used to limit the inrush current during startup [15], [16], to keep the switching frequency in vicinity of the resonance frequency [17], and to limit the maximum switching frequency for low load conditions [18]-[20]. In limited number of the studies, these two methods have been used together [21]-[23]. In [21], the frequency modulation is applied for normal operation condition. When the load is lower than a specific value, the frequency modulation and phase-shift control are applied together. Here, the phase-shift angle is obtained by using a linear equation of the load current and the output voltage is regulated by the frequency modulation method. However, this combined control is only applied for light-load condition. In [24], a hybrid modulation technique combining frequency modulation and pulse density modulation has been proposed. However, these two methods have not been applied together. The pulse density modulation is used to limit the switching frequency at a determined limit. In [25], a lookup table-based optimal phase-shift and frequency detection method is proposed for a battery charger application. When the frequency modulation and phase-shift method are applied together, the same output voltage and current value can be obtained with different frequency and phase-shift values. The derived model is used to calculate converter losses, and optimal phase-shift and frequency values providing the lowest loss value are determined and saved in lookup tables (one for frequency and one for phase-shift) for different output voltage and current conditions. However, only converter losses are considered, and transformer losses are ignored. In addition, along with the optimal phase-shift value, to track the reference signal and remove the error, an additional phase-shift value is obtained with a proportional-integral (PI) controller, and total phase-shift value is obtained by adding this value to the calculated optimal phase-shift value. Thus, the actual phase-shift value applied to the converter is not the calculated optimal phase-shift value. Although, efficiency values are only reported for a voltage level, the maximum reported efficiency is about 91%. This clearly shows that transformer loss should be also considered. To the best of authors knowledge, optimal determination of phase-shift and switching frequency values depending on the operation point and considering the complete system has not been discussed yet.

In this study, a high-frequency-link photovoltaic (PV) inverter is proposed. The block diagram of the proposed inverter topology is given in Fig. 1(c). Here, the isolated dc–dc converter stage is controlled to generate the rectified sine wave voltage and current at the dc bus. Different from the topology given in Fig. 1(b), the grid-side inverter circuit operates at line frequency and only inverts the rectified sine wave voltage and to the ac current. All the current control and regulation actions are performed through the dc-dc converter stage. Thus, the high-frequency switching requirement at the grid side and related switching losses are removed. This makes the proposed system suitable for the direct connection to the MV grid. The LLC resonant converter is designed for this dc-dc converter stage. A combined modulation scheme employing both frequency modulation and phase-shift control methods is applied to control the current and to generate rectified sine waveform at the dc bus. The ZVS boundary and losses of the power converters and transformer with the proposed combined modulation scheme are investigated. Then, an optimal trajectory that gives the optimal switching frequency and the phase-shift angle values is determined by using the Lagrange

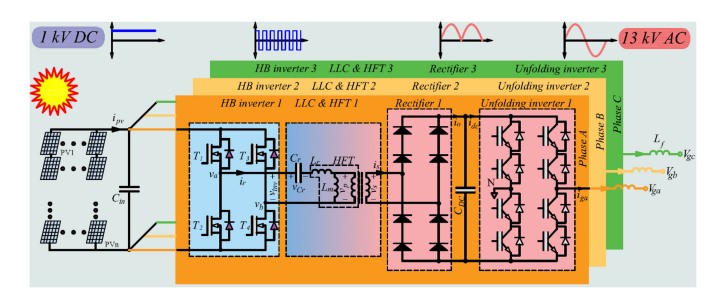


Fig. 2. Detailed circuit of the proposed solar PV inverter.

multiplier method and considering the power converters and transformer losses and the ZVS boundary to achieve highest efficiency for any operation point. The conventional LFT is replaced by an HFT, and thus, a high power dense and efficient system design is obtained. With the proper design of the transformer, the leakage inductance of the transformer is used as resonant inductor, additional inductor requirement is removed, and circulating current and related losses are limited. The proposed system and effectiveness of the suggested optimal trajectory is verified with MATLAB/Simulink simulations and experimental studies.

## II. PROPOSED SOLAR PV INVERTER TOPOLOGY

Large-scale PV systems are usually connected to MV grids through LFTs to step up the output voltage to the MV and provide galvanic isolation. Since these LFTs have some drawbacks such as higher cost, loss, and size, a novel concept and topology for the solar PV inverter connected to the MV grid is proposed in this study. This topology removes the LFT and instead employs a medium-frequency transformer embedded into the dc-dc converter. The circuit diagram of the proposed topology is shown in Fig. 2. This topology enables a direct MV penetration of the PV system with a higher efficiency, higher compactness, and lower cost. The *LLC* converters are used to generate rectified sine wave voltages and current at the MV dc bus. The current regulation and control and maximum-power-point-tracking (MPPT) actions are performed by these LLC converters. They also provide a ZVS for primary-side switches and a ZCS for secondary-side diodes for a wide operation area and decrease the losses. Besides, the buck or boost mode operation capability of the *LLC* resonant converter extends the MPPT range. The unfolder inverter operates at the line frequency and only inverts the dc bus current formed by the LLC resonant converter into the sine wave current. Thus, the high-frequency switching requirement at the MV side is removed. Besides, the proposed system provides a more compact and efficient design by removing the bulky LFT.

## A. LLC Resonant Converter

In last two decades, high efficiency and high power density requirements have increased the number of studies on *LLC* resonant converters. These converters are basically in serial resonance converter structures and widely used in isolated dc–dc converter applications in consumer electronics. They have superior advantages among the resonant converters such as operation

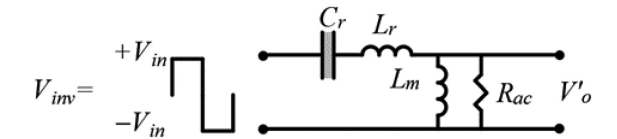


Fig. 3. Simplified model of the *LLC* resonant converter.

in a boost or buck modes capability, high power density, dc component blocking capability, providing wide input voltage and load ranges, achieving ZVS at primary side switches and ZCS at secondary side diodes, low electromagnetic interference (EMI), etc. [26]–[29]. But, the *LLC* converters have some drawbacks such as, difficulties on regulating the output voltage at no-load condition, loosing ZVS at low-load conditions, and difficulties in analysis [30], [31].

A simplified circuit of the *LLC* resonant converter can be depicted as in Fig. 3. Here,  $R_{\rm ac}$  is the *LLC* converter load value reflected from the secondary side of thr transformer to thr primary side and can be calculated as  $R_{\rm ac}=R_o8n^2/\pi^2$ , here,  $R_o$  is the actual converter load;  $V_o'$  is the output voltage, which is transferred to the primary side; n is the turn ratio, and  $L_m$  is magnetizing inductance of the transformer. The resonance frequency  $(f_{r1})$  of this circuit can be written as

$$f_{r1} = 1/(2\pi\sqrt{L_r C_r}). {1}$$

Then, the voltage equation can be obtained as

$$v_{\text{inv}}(t) = \begin{cases} -V_{\text{in}}, & -\frac{T}{2} \le t < 0\\ V_{\text{in}}, & 0 \le t < \frac{T}{2} \end{cases}$$
 (2)

$$v_{\rm inv}(t) = \sum_{k=1}^{\infty} \frac{4V_{\rm in}}{k\pi} \sin\left(k\omega_s t\right) \tag{3}$$

where  $\omega_s$  is the angular switching frequency. By using first harmonic approximation, quite useful and common method, (3) can be rewritten as follows for k = 1 [26]:

$$v_o'(t) = \frac{4V_{\rm in}}{\pi} \sin\left(\omega_s t\right). \tag{4}$$

In addition, the input impedance relationship can be found easily from Fig. 3 as

$$Z_{\text{in}} = \begin{cases} Z_{Cr} + Z_{Lr} & \text{for } R_{\text{ac}} = 0\\ Z_{Cr} + Z_{Lr} + Z_{Lm} / / R_{\text{ac}} & \text{for } 0 < R_{\text{ac}} < \infty\\ Z_{Cr} + Z_{Lr} + Z_{Lm} & \text{for } R_{\text{ac}} = \infty. \end{cases}$$
(5)

It can be seen from (5) that different resonant tanks occur in the converter for different operation conditions. When no energy is transferred from the primary side to the secondary side,  $L_m$  and  $L_r$  are serially connected and resonate with  $C_r$ , and define a second resonant frequency value. In other words, during a switching period, in addition to the  $f_{r1}$ , another resonance frequency is appeared. The effect of the transformer magnetization inductance and load level determine which resonant frequency is dominant in the system. This second resonance frequency can be expressed by the following equation:

$$f_{r2} = 1/(2\pi\sqrt{(L_r + L_m)C_r}).$$
 (6)

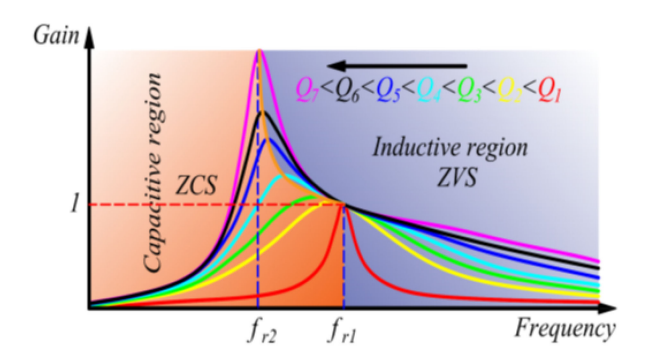


Fig. 4. Relationship between gain and frequency.

The resonant tank impedance that has major effect on the *LLC* converter operation can be written as follows by substituting variables into (5):

$$Z_{\rm in} = \sqrt{\frac{L_r}{C_r}} \left( \frac{f_n^2 Q}{L_n^2 + f_n^2 Q^2} + j \left( \frac{f_n L_n}{L_n^2 + f_n^2 Q^2} - \frac{1 - f_n^2}{f_n} \right) \right).$$
(7)

It is clear from (7) that the switching frequency, which can be determined by the designer, and the load are two major parameters effective on the resonant tank impedance with assumption of tank components' parameters are constant. The effect of the load is represented by a parameter called quality factor (Q) given as follows:

$$Q = \frac{\sqrt{\frac{L_r}{C_r}}}{R_{\rm ac}}.$$
 (8)

The gain of the *LLC* resonant converter  $(\frac{|V_{in}|}{|V'_o|})$ , which is dependent on the resonant tank parameters, the switching frequency, and the load can be expresses as:

$$M(Q, m, f_n) = \frac{(f_n^2(m-1))}{\sqrt{(mf_n^2 - 1)^2 + f_n^2(f_n^2 - 1)^2(m-1)^2Q^2}}$$

where m and  $f_n$  are the inductance factor and the normalized frequency values, respectively, and they are defined as follows:

$$m = \frac{L_m + L_r}{L_r} \tag{10}$$

$$f_n = \frac{f_s}{f_{r1}}. (11)$$

It is worth to note that the output voltage is only related to the input voltage, the switching frequency, and the load value. Thus, the frequency modulation method based on controlling the switching frequency have been proposed and widely used to control the output voltage of the LLC converters [32]. Generally, the switching frequency is controlled to obtain  $f_n < 1$  for the boost mode operation and  $f_n > 1$  for the buck mode operation. However, when the variation of the gain versus switching frequency is plotted for different quality factor, as given in Fig. 4, it is seen that there are constraints for both operation modes to obtain required gain values.

The m value is another important factor that defines the operation characteristics of the converter. The larger m value refers to a wider region between  $f_{r1}$  and  $f_{r2}$ . In addition, the

larger m value reduces the circulating current and decreases the losses. However, the higher m (or magnetizing inductance) value increase the required switching frequency to provide same attenuation at the output voltage. Moreover, the higher values of the magnetization inductance can obstacle to discharging the switch capacitance ( $C_{\rm oss}$ ) and even cause to lose ZVS operation when dead time is not big enough, and increase power loss [33], [34]. So, the effect of each parameter should be considered.

## B. ZVS Analysis

One of the major advantages of the *LLC* resonant converter is providing inherited ZVS turn ON for primary-side switches. Two key factors are effective on achieving ZVS. The first one is the switching frequency. It is seen from Fig. 4 that there are three different operation regions depending on the resonant tank impedance. The inductive resonant tank inductance and the lagging resonant current discharges the output capacitors of the switches and provide ZVS for the primary-side switches [35], [36]. Therefore, the following can be written as a first constraints of the ZVS

$$\theta = \arctan\left[-\frac{f_n^4 Q^2 + f_n^2 L_n^2 + f_n^2 L_n - f_n^2 Q^2 - L_n^2}{f_n^3 Q}\right]. \tag{12}$$

The second constraint is about the dead-time and transformer magnetizing current. As mentioned previously, the switch and parasitic capacitances should be discharged until the end of the dead-time period by the resonant tank current that equals to the transformer magnetizing current during this interval [35]. Therefore, the magnetizing current should be high enough (or in other words, the dead time should be long enough) to discharge the capacitances during the dead time to achieve the ZVS operation. However, higher magnetizing current values increase the circulating current and losses. Therefore, its design is very important. The second condition to achieve ZVS can be written as follows in terms of switch and parasitic capacitances and magnetizing charge

$$Q_m \ge 2C_{\text{pri}_{os}}V_{\text{in}} + (C_{\text{stray}} + C_W)V_{\text{in}} + \frac{1}{n}C_{\text{sec}_{os}}2V_o.$$
 (13)

where  $Q_m$  is the charge provided by the magnetizing current,  $C_{\mathrm{pri}_{os}}$  is primary side device's output capacitance,  $C_{\mathrm{sec}_{os}}$  is secondary side device's output capacitance, n is the transformer's turns ratio, and  $C_{\mathrm{stray}}$  and  $C_W$  are the stray capacitance of the printed circuit board layout and winding capacitance of the transformer, respectively.

The charge provided by the transformer magnetizing current can be written as follows:

$$Q_m = I_{Lm_{nk}}(V_{\text{in}})t_d \tag{14}$$

where  $I_{Lm_{pk}}(V_{\rm in})$  is the peak value of the magnetizing current, which is a function of the input voltage  $V_{\rm in}$  and dead-time  $t_d$ . Also,  $I_{Lm_{pk}}(V_{\rm in})$  can be expressed as follows:

$$I_{Lm_{pk}}(V_{\text{in}}) = \frac{1}{2} \frac{V_{\text{in}} \frac{T_r}{2}}{L_m} = \frac{V_{\text{in}}}{4L_m f_{r1}}.$$
 (15)

TABLE I CORE MATERIAL CHARACTERISTICS

Core	Power	Operating	$B_{max}$	Cost	Market
Material	Loss	Temp.			
Ferrite	Low	Low	Moderate	Low	High
Si-Steel	High	Moderate	High	Low	High
Nanocrystalline	Low	High	High	High	Low
Amorphous	High	Moderate	High	Moderate	High

By combining (14) and (15), the required dead time to achieve ZVS can be derived as in (16):

$$t_{d_{\text{required}}} = \frac{4L_m f_{r1} Q_m}{V_{\text{in}}}. (16)$$

## C. Medium-Frequency Transformer Design

In the design process, type of the core material, the core geometry, and the core size are important parameters that should be considered according to targeted frequency and power level. As it is well-known, materials such as Ferrite, Nanocrystalline, Si-Steel, and Amorphous are frequently used in medium- and high-frequency transformer designs as core materials. Ferrite and Nanocrystalline are preferred at medium and high frequency to minimize core losses and to reach higher efficiency. The saturation level of the Nanocrystalline material is higher than the Ferrite. However, when the frequency increases, its losses become higher, and Ferrite becomes more advantageous. A comparison of the core materials is given in Table I.

The core cross-sectional area  $(A_c)$  and the window area  $(W_a)$  are the basic parameters in core size determination. The product of the effective core cross-sectional area  $(cm^2)$  and the window area  $(cm^2)$  given as follows  $(A_p)$  is the basic mechanical parameter  $(cm^4)$  for the transformer

$$A_p = A_c W_a = \frac{S}{K_f K_{\rm cu} B_{\rm max} f J} 10^4$$
 (17)

where S is the rated power (VA),  $K_f$  is the waveform coefficient of the excitation voltage,  $K_{\rm cu}$  is the window utilization coefficient of the windings,  $B_{\rm max}$  is the maximum flux density, f is the operating frequency of the transformer, and J is the current density. The induced voltage on transformer windings can be found via one of Faraday's Law as follows:

$$v(t) = N\frac{d\phi(t)}{dt} = NA_c \frac{dB(t)}{dt}$$
(18)

where v(t) represents the instantaneous value of the induced voltage, B(t) is the magnetic flux density,  $\phi(t)$  is the magnetic flux, and N is the number of turns. Solving (18) for B(t) gives the magnetic flux density

$$B(t) = \frac{1}{4} \frac{E}{NA_c f} \tag{19}$$

Then, the aforementioned equation can be rewritten for partial square wave with dead time  $(t_d)$  to obtain  $B_{\text{max}}$  and number of

turns, respectively as follows:

$$B_{\text{max}} = \frac{1}{2} \frac{E}{NA_c} \left( \frac{T}{2} - t_d \right) \tag{20}$$

$$\times N = \frac{E}{K_f B_{\text{max}} A_c f} \left( 1 - \frac{t_d}{\pi} \right) \tag{21}$$

where T is the period of the switching cycle. As can be seen from (20) and (21), the number of turns, the frequency, and the magnetic flux density, and the core cross-sectional area interact with each other. On the other hand, the frequency and the magnetic flux density have an impact on core loses. The Steinmetz's equation given in (22) is commonly used in the calculation of core losses of the transformers depending on the switching frequency,  $f_s$  as well as flux density, B as follows:

$$P_c = k_c f_s^{\alpha} B^{\beta} \tag{22}$$

where  $P_c$  is core loss for unit volume, and  $k_c$ ,  $\alpha$ , and  $\beta$  are core coefficients that can be found in the manufacturer's datasheet.

Besides the selection of the core material, the core type must be specified. Although it is possible to see different types of core structures, core-type and shell-type structures are commonly used. Shell-type transformers have the advantage of lower leakage inductances, and the core-type transformers provide thermally better winding arrangement. Since the LLC resonant converter topology needs a resonant inductance, by appropriate design, the leakage inductance of the transformer can be used as resonant inductor, and thus, an additional inductor requirement is removed. Therefore, selection of the transformer core type and determining the desired leakage and magnetization inductance are important design parameters. However, a tradeoff have to be made between parameters such as the number of turns, core cross-sectional area, frequency, and efficiency. For this purpose, some theoretical analysis and simulation studies have been carried out through MATLAB as explained in [37]. In the design phase, along with the other parameters, the leakage and magnetizing inductance values are also considered to remove the additional inductance requirement, and reduce the circulation current and related power loss. Then, finite-element analysis (FEA) method-based software are used to simulate the system. The designed transformer can be simulated with power electronic converters to achieve more accurate results. According to the simulation results, the design can be revised. When desired results are obtained, the designed transformer is implemented and tested [38]. These details are not given due to the page limitation. After an extensive study, it was concluded that the Ferrite MnZn 3C94 material from Ferroxcube is the best choice in terms of the frequency range, the flux density, and the total power loss. To achieve the optimum core crosssectional area and window area, "U" shape cores U93/76/30 mm (width/height/depth) are used to build the transformer core. In order to determine the appropriate conductor cross section area at high frequency transformer designs, the skin effect has to be considered. Therefore, a Litz wire is used in transformer windings. As a result of the calculations, 8AWG Litz wire has been chosen, which is composed of number of 38AWG

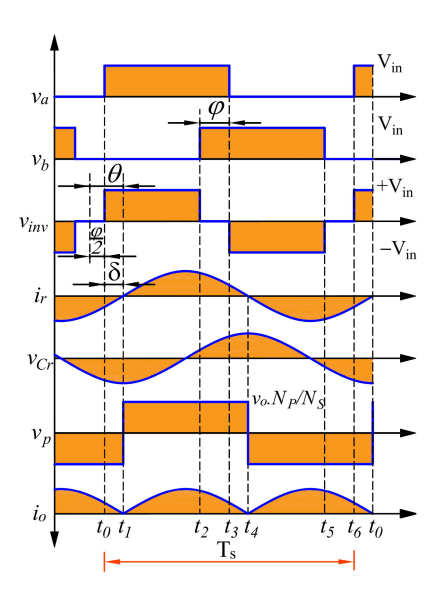


Fig. 5. Current and voltage waveforms of a phase-shift-controlled *LLC* resonant converter.

strands. Then, FEA method-based software is used to simulate the system.

### III. CONTROL SCHEME OF THE PROPOSED SYSTEM

As it is seen form (9) that the output voltage of the *LLC* resonant converter can be controlled with switching frequency and input voltage. In this study, the LLC resonant converter is employed in a grid-connected inverter as given in Fig. 1(c). Since the grid-side inverter stage is operating at line frequency as an unfolder, the *LLC* converter has to regulate and shape the dc bus voltage and current in a rectified sine wave. Thus, the voltage gain of the LLC converter has to be reduced down to zero. This is practically impossible with only switching frequency control. Therefore, the phase-shift control is also employed. In this control method, the duty ratio values of the switching signals are kept as 50%, and a phase-shift ( $\varphi$ ) is added between the switching signals of two legs of the full-bridge inverter as depicted in Fig. 5. Here, although its waveforms depends on the tank parameters, the switching frequency, and the phase-shift angle, the resonant current is assumed as sinusoidal. Similarly, since the switching frequency is much higher than the line frequency, the output voltage is assumed as constant dc voltage when showing the transformer primary voltage. In this control mode, the fundamental component of the resonant tank's supply voltage can be written as in (23) dependent to the phase-shift

$$v_{\text{inv}_1} = v_o'(t) = \frac{4V_{\text{in}}}{\pi} \sin \frac{\pi - \varphi}{2} \sin (2\pi f_s t), \quad 0 \le \varphi \le \pi.$$
(23)

It is seen that this method brings another component to the gain function by controlling the input voltage.

As it is explained in previous section, inductive resonant tank impedance is one of the ZVS constraint. For the traditional *LLC* resonant converter with frequency modulation, this condition is fulfilled if the switching frequency is higher than the resonant

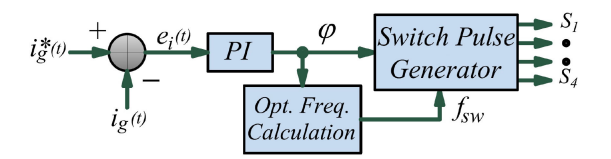


Fig. 6. Block diagram of the proposed control scheme.

frequency. However, in case of phase-shift control, the constraint should be modified. A higher phase-shift angle may cause a leading resonant current, which means capacitive mode operation even when the switching frequency is higher than the resonant frequency value. The resonant tank impedance angle and the phase-shift angle are two parameters that define the operation mode as inductive or capacitive. The phase angle between the resonant current and input voltage is given follows:

$$\delta = \begin{cases} \theta, & \text{for } \varphi = 0\\ \theta - \frac{\varphi}{2}, & \text{for } 0 < \varphi \le \pi \end{cases}$$
 (24)

where  $\theta$  is the phase angle of the resonant tank impedance. It is clear that the ZVS angle  $(\delta)$  has to be positive to guarantee the ZVS. In this study, the phase-shift angle has to be controlled from 0 to  $\pi$  to generate a rectified sine wave output current. Therefore, achieving ZVS for whole operation area is theoretically impossible. The ZVS operation range is related about the angle of the resonant tank impedance, and higher values of the impedance angle provide a wider ZVS operation range. As it is seen from (12) that higher m value enables this. However, increasing  $L_m$  may also cause losing ZVS according to the second constraint given in (13).

According to Fig. 5 and (24), around the zero crossings of the reference current signal, the resonant current starts to lead the resonant tank voltage. In this condition, the LLC converter loses the ZVS operation. In past literature, it is mentioned that leading resonant current may cause MOSFET failures because of the body diode reverse recovery charges. The reverse recovery charge has direct relation with the current value and reverse recovery charge value of the switches. Since the proposed system only operates with leading current around zero crossings, the current value at switching intervals is small. In addition, new generation SiC MOSFETs with a lower reverse recovery charge also help this operation mode. It is reported that while reverse body diodes' recovery charge of the SiC MOSFET is 0.120 [39] and 0.192  $\mu$ C [40], the counterpart Si MOSFET has a 2- $\mu$ C reverse recovery charge. These two situations remove the risk of the MOSFET failures in capacitive region because of the body diodes' reverse recovery charge.

The block diagram of the proposed control scheme is depicted in Fig. 6. It is seen that there are two control variables, the switching frequency and phase shift. The phase shift is calculated according to the current error by the PI controller. The Ziegler–Nichols method is applied to determine the PI controller gains. The output of the PI controller can be expressed as follows:

$$\varphi(t) = K_P[i_g(t) - i_g(t)^*] + K_I \int [i_g(t) - i_g(t)^*] dt$$
 (25)

where  $i_g(t)$  is the system output current injected to the grid and  $i_g(t)^*$  is its reference signal. Thus, the phase-shift angle is determined. However, for any instant, various phase-shift angle-switching frequency pairs are capable of providing same converter gain. Here, an optimization method can be employed to calculate the frequency according to the phase-shift angle to minimize the losses of the converter. The details of the optimization process and generation of the optimal trajectory are given in Section IV. The obtained trajectory is used to calculate the switching frequency for any operating point.

# IV. OPTIMAL RELATION BETWEEN THE PHASE SHIFT AND SWITCHING FREQUENCY

The output power can be controlled with both the phase-shift angle and switching frequency. This article suggests a method to find the optimal phase-shift angle and switching frequency pair in order to keep the overall converter and transformer losses at possible minimum value. The gain function between the output voltage and the input voltage is given as follows:

$$M = \frac{V_o}{V_i} = \frac{nf_n^2(m-1)\sin\left(\frac{\pi-\varphi}{2}\right)}{\sqrt{(mf_n^2 - 1)^2 + f_n^2(f_n^2 - 1)^2(m-1)^2Q^2}}.$$
 (26)

The output power is written in (27). The power is sensitive to the phase-shift angle and it also varies by changing the switching frequency especially at the low phase-shift region.

$$P_{\text{out}} = \frac{V_o^2}{R_e} = \frac{V_i^2 M^2}{R_e}.$$
 (27)

In this study, the losses are considered to be sum of conductive losses  $(P_w)$ , core losses of the transformer  $(P_c)$ , and the switching losses of the inverter  $(P_s)$ . The resonant current,  $I_r$ , is the input current of the transformer and can be calculated by (28). The conduction loss of the inverter and the copper loss of the transformer are calculated from  $I_r$  by (29), where  $R_t$  is the total resistance.

$$I_r = \left| \frac{4}{\pi} V_i \sin \left( \frac{\pi - \varphi}{2} \right) \frac{1}{\left( \left( \frac{1}{j\omega_s C_r} + j\omega_s L_r \right) + \left( \frac{j\omega_s L_m R_e}{j\omega_s L_m + Re} \right) \right)} \right|$$
(28)

$$P_w = R_t I_r^2. (29)$$

After examining the switching loss data given in datasheet and switch characterization test results, it is seen that a quadratic function of the current can be written to describe the switching loss depending on the switching frequency and the current as shown in (30). The coefficients of the quadratic equation obtained from the curve fitting on the loss curves obtained from datasheets and switch characterization tests.

$$P_s = (aI_r^2 + bI_r + c)f_s. (30)$$

In addition, as it can be seen from Fig. 5, the instantaneous value of the resonant current (converter current) at switching interval depends on the angle ( $\delta$ ) between the inverter output voltage and resonant current. According to (12) and (24),  $\delta$  also depends on the switching frequency and phase-shift angle. Therefore, the switching frequency and phase-shift angle have effect on

switching losses and have to be considered. Consequently, (30) is modified as as follows:

$$P_s = (aI_r(f_s, \phi)^2 + bI_r(f_s, \phi) + c)f_s.$$
 (31)

Furthermore, as explained in (24), the ZVS operation during turn ON can be achieved if  $\delta \geq 0$ . For higher values of the phase-shift angle (around the zero crossings of the grid current), the ZVS operation is lost. Therefore, the proposed *LLC* resonant converter would have different switching loss characteristics. In the optimization process, the ZVS boundary that depends on the resonant tank parameters, the switching frequency, and the phase-shift angle is defined and considered in switching loss calculations. The Steinmetz's equation, given in (22), is commonly used in calculation of core losses of the transformers depending on the switching frequency as well as the flux density. However, B depends on the voltage applied to the transformer, which varies with frequency and phase-shift angle. According to Faraday's Law ( $V = -N \mathrm{d}\phi/\mathrm{d}t$ ), the maximum flux density for the proposed modulation strategy can be obtained as

$$B_{\text{max}} = \frac{\frac{4V_i}{\pi} \sin\left(\frac{\pi - \varphi}{2}\right)}{2\pi f_s N A_c} \tag{32}$$

where  $B_{\rm max}$  is the maximum value of the flux density,  $A_c$  is the core cross-sectional area, and N is number of turns. The total loss  $(P_{\rm loss})$  of the system is given as follows:

$$P_{\text{loss}} = P_w + P_s + P_c. \tag{33}$$

Components of the losses and the total loss, the ZVS boundary and the ZVS angle ( $\delta$ ) are depicted in Fig. 7. Here, the maximum value of the switching frequency is limited depending on the switches' and core's operating frequency limitations. As seen previously, the core losses and switching loss both depend on phase-shift angle and switching frequency values. Therefore, for a given operating point, different phase-shift angle and switching frequency values can give the same total gain with different loss effects.

Since the converter gain has to be reduced down to 0, and this is only possible with phase-shift control, first the phase-shift angle is determined by the current controller to track the reference signal. Then, an optimum switching frequency value for this phase shift is searched. The total loss given in (33) is defined as the objective function, which is needed to be minimized. To find the optimal trajectory of the switching frequency for the whole range of power or phase-shift angle, the Lagrange multiplier method, which is an excellent tool to find the minimum/maximum of an objective function subject to satisfy the constraint, is used. Based on the Lagrange multiplier, an objective function  $f(\varphi, f_s) = P_{\text{loss}}$ , and a constraint function  $g(\varphi, f_s) = P_{\text{out}}$ , both in terms of independent variables  $\varphi$  and  $f_s$  can be written as

$$\Lambda(\varphi, f_s, \lambda) = P_{loss} + \lambda P_{out} \tag{34}$$

where  $\lambda$  is Lagrange multiplier variable. To find Lagrange equation, which is the trajectory of the optimum curve on the  $\varphi-f_s$  plane, the partial derivative of the optimization function should

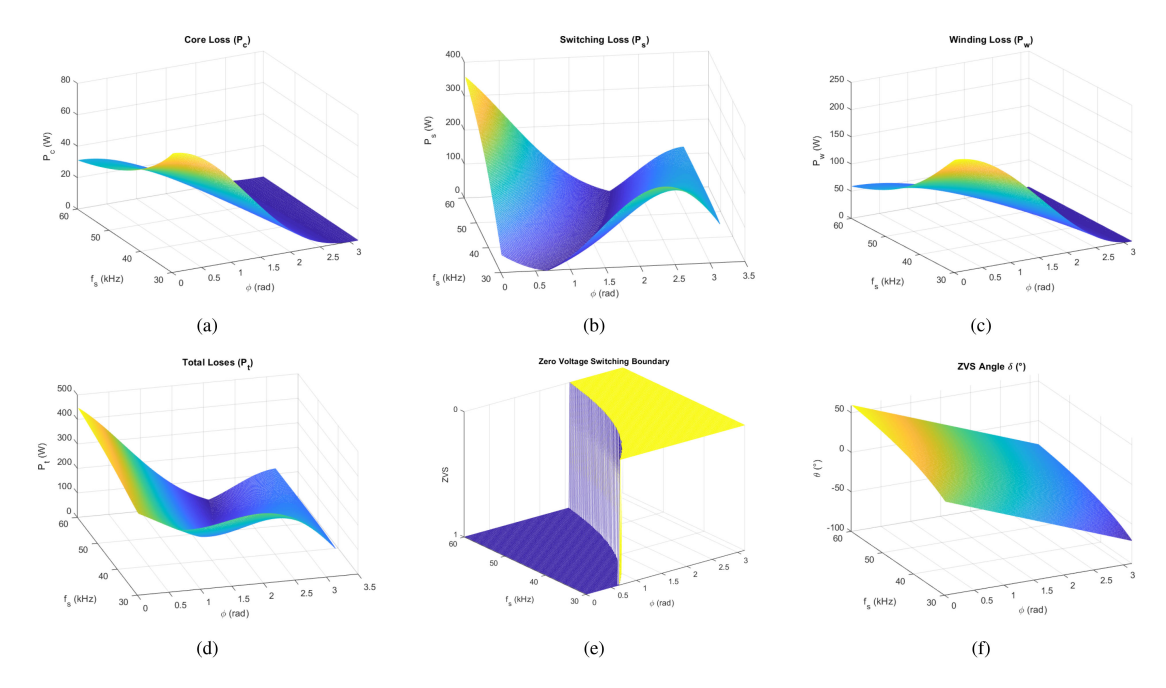


Fig. 7. (a) Core losses. (b) Switching loss. (c) Winding and conduction losses. (d) Total loss. (e) ZVS boundary. (f) ZVS angle.

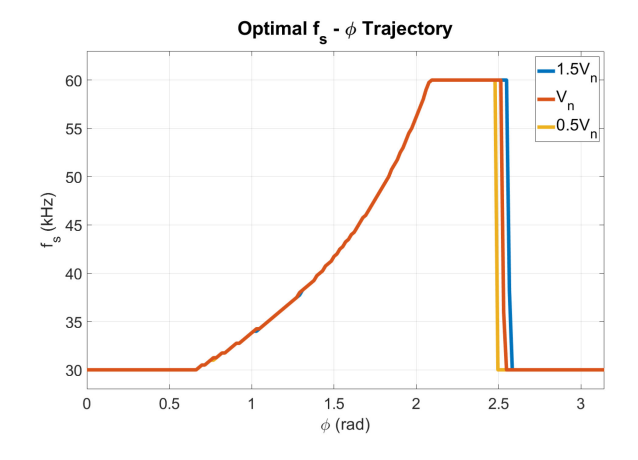


Fig. 8. Optimal trajectory for different input voltage levels considering switching frequency constraint.

be equal to zero.

$$\frac{\partial \Lambda}{\partial \varphi} = \frac{\partial P_{\text{loss}}}{\partial \varphi} + \lambda \frac{\partial P_{\text{out}}}{\partial \varphi} = 0$$
 (35a)

$$\frac{\partial \Lambda}{\partial f_s} = \frac{\partial P_{\text{loss}}}{\partial f_s} + \lambda \frac{\partial P_{\text{out}}}{\partial f_s} = 0.$$
 (35b)

To find Lagrange equation,  $\lambda$  should be eliminated between the first and second equations to find the relation between  $\varphi$  and  $f_s$ . The optimal trajectory of Fig. 8 is obtained after eliminating  $\lambda$  in (35). It suggests a switching frequency value to keep the losses at the minimum for any phase-shift determined by the controller. It is seen that, the optimal trajectory offers keeping switching frequency at lower limit (30 kHz), because the phase-shift angle at this point is low and the system can achieve ZVS turn ON with this frequency. However, after a certain value of the phase-shift angle, the switching frequency should be increased to sustain the ZVS turn ON as seen in the figure. As explained before, to achieve ZVS turn-ON operation, the angle  $(\delta)$  between the resonant current and resonant tank input voltage, given in (24),

should be positive. However, achieving ZVS for whole operation range is impossible as depicted in Fig. 7(e). Here, while "1" is representing the soft-switching region, and "0" represents the hard-switching region. Increasing frequency extends the ZVS range, however, because of the switches and core material limitations, a maximum frequency limit has to be determined. Even after ZVS is lost, a higher switching frequency helps to keep the phase angle around the zero crossings of the voltage and current signals lower. This results with a lower current value at the switching intervals and leads lower switching losses. Therefore, the switching frequency is kept at its maximum value for a while after the ZVS is lost. After a certain value, because of the increase in the switching loss, the optimization algorithm offers to decrease the switching frequency. At this point, since higher switching frequency increases losses, lower switching frequency provides a better efficiency. The proposed optimization process is tested for different input voltage conditions, and optimal trajectories for  $0.5V_n$ ,  $V_n$  (nominal voltage), and  $1.5V_n$ are also depicted in Fig. 8. As it is seen from the figure, the first (30-kHz region) and second (variable frequency region) parts of the optimal trajectories are the same for all three input voltage values. The only difference is the starting point of the third part (60-kHz region). It is clear that an additional compensation can be easily added to the switching frequency calculation to add input voltage adjustment. This also proves that the proposed system is suitable to use in wide input voltage range applications.

## V. SIMULATION AND EXPERIMENTAL RESULTS

The validation of the proposed *LLC* resonant converter-based solar PV inverter is performed by simulation and experimental studies. The proposed system is modeled with MAT-LAB/Simulink. The additional resonant inductor requirement is removed, and the leakage inductance of the transformer is used as a resonant inductor by the proper transformer design. Besides, since the major control variable for adjusting the gain

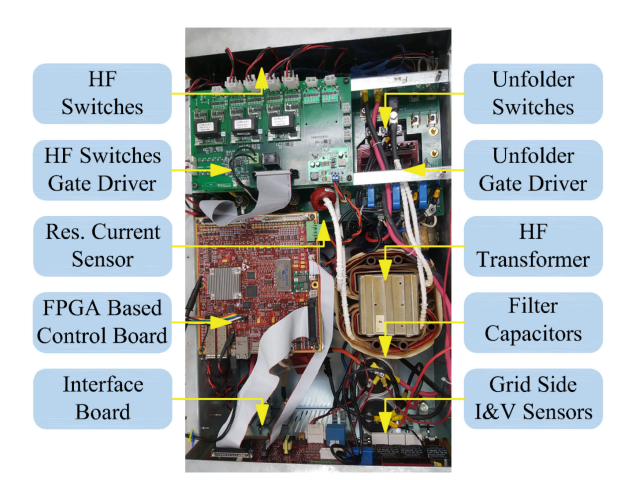


Fig. 9. Designed prototype.

#### TABLE II System Parameters

Symbol	Value	
Resonant Inductor, $L_r$	8uH	
Resonant Capacitor, $C_r$	4uF	
Magnetizing Inductance, $L_m$	250uH	
Supply Voltage, $V_{in}$	200V	
Transformer Turn Ratio, $n$	1:1.1	
Switching Frequency, $f_s$	30 - 60kHz	
Grid Voltage and Frequency, $V_g$ , $f_g$	110V, 60Hz	

is the phase-shift angle, bigger m value is targeted to limit the circulation currents and reactive power, and achieve a higher efficiency. The resonant frequency and switching frequency range is determined to be suitable for medium power systems. The resonant capacitor is selected according to the resonant frequency target and resonant current value. The turn ratio of the transformer is selected as 1.1 to provide voltage matching between the dc voltage and the grid voltage level by considering the voltage drops on power switches and transformer windings. The evaluation of the input signals, control actions, and pulsewidth modulation (PWM) generation were implemented by using Altera FPGA. The analog signals were read by AD7328 analog-to-digital converter (ADC) chips (1MSPS, 12-bit, eight input channels), current transformers, and resistive voltage dividers. The voltage and current transducer and ADC chips are selected according to the switching frequency range, voltage, and current amplitudes. The designed prototype, rated to 3.8 kW, is shown in Fig. 9 and its main parameters are given in Table II.

In the proposed system, both the phase-shift and the switching frequency values are controlled at any instant to regulate the dc bus current by modulating the resonant current. While the controller determines the phase-shift angle to track the reference signal and generate the rectified sine wave current at the dc bus, the optimal trajectory determines the optimum switching frequency value depending on the phase-shift angle to control the dc bus current with optimum efficiency. The simulation and experimental results of the grid voltage  $(v_g)$ , the current injected to the grid  $(i_g)$ , resonant current  $(i_r)$ , and the dc bus current  $(i_{dc})$ 

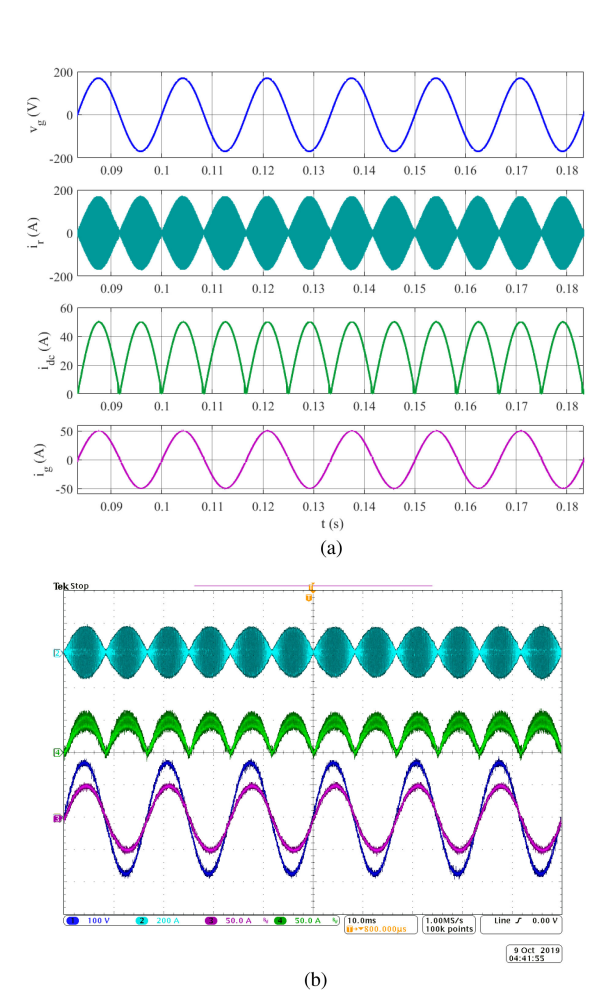


Fig. 10. Simulated and experimental waveforms of  $v_g$ ,  $i_g$ ,  $i_r$ , and  $i_{dc}$ , resonant current, and dc current. (a) Simulation. (b) Experiment (CH1 ( $v_g$ ): 100 V/div, CH2 ( $i_r$ ): 200 A/div, CH3 ( $i_g$ ): 50 A/div, and CH4 ( $i_{dc}$ ): 50 A/div).

are shown in Fig. 10. It is clearly seen that the proposed converter topology and control scheme with optimal trajectory generates a rectified sine wave current at dc bus, and injects sinusoidal current to the grid. The total harmonic distortion (THD) level of the current injected to the grid is measured as 2.62%. It provides a good control performance in terms of power quality, which is an important performance index defined by international standards for grid-connected inverters.

In Fig. 11, the simulation and experimental results for the grid voltage, the resonant current, and the dc bus current generated by the *LLC* resonant converter are shown. The PWM signals for both inverter legs captured form experimental set up are also given. An abrupt change is applied to the reference current signal and its value is increased from 40% to 100% of its rated value to test the dynamic response of the system. It is clearly seen from both simulation and experimental results that the dc bus current tracks its reference value with a fast response and without any oscillations and overshoot. It is worth to note that besides efficiency optimization, the proposed system also provides a good dynamic response. The resonant current waveforms are also given in Fig. 12 for different phase-shift angle values.

The ZVS turn-ON capability of the proposed system is also investigated. As mentioned before, achieving ZVS for whole

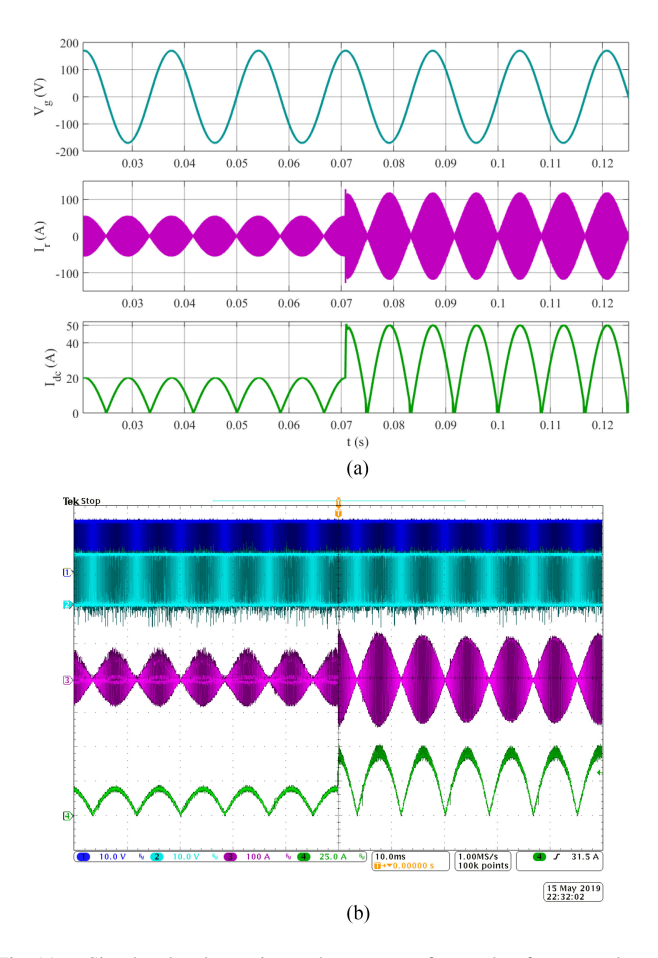


Fig. 11. Simulated and experimental responses of  $i_{\rm dc}$  and  $i_r$  for a step change in  $i_{\rm dc}$  from 20 to 50 A. (a) Simulation. (b) Experiment (CH1  $(v_{G1})$ , CH2  $(v_{G2})$ : 10 V/div, CH3  $(i_r)$ : 100 A/div, and CH4  $(i_{\rm dc})$ : 25 A/div).

operation range is impossible but by appropriate design of the transformer inductances and frequency control, the ZVS operation range can be extended. As explained with (24) and depicted in Fig. 7(e), the ZVS boundary varies with the switching frequency and it is possible to extend it with increasing frequency. While the highest phase-shift value that the ZVS turn ON can be achieved is around 60°, it is increased to around 120° by increasing the switching frequency to 60 kHz. This gives 0.49 gain within the ZVS boundary. Besides, the frequency modulation (increase in frequency) provides another gain, which is around 0.505-0.0445 depending on the Q value. Combinational use of these two methods provides around 0.3 gain at the ZVS boundary. Fig. 13 shows the grid voltage  $(v_q)$ , the drain-to source voltage  $(v_{DS})$  of one of the upper switch, and the grid current  $(i_q)$  and the resonant current  $(i_r)$  waveforms around this ZVS boundary. Three different instants are given to see the inductive and capacitive current situations. The oscillation on  $v_{\rm DS}$  appears at the turn-OFF instant of other upper switch and is not related about the ZVS status. As explained in Section II-B, the inductive current is one of the ZVS constraints. In this mode, the resonant current should change its polarity before the switch is turned ON. One can easily see that while the resonant current is capacitive and the ZVS is lost in Fig. 13(a), the inductive resonant current condition is obtained and ZVS turn ON achieved in Fig. 13(c). The instant given in Fig. 13(b) is almost the ZVS boundary

condition. In Fig. 14, experimental waveforms of PWM signals for inverter upper switches, resonant network voltage, and dc bus current are shown. The experimental waveforms shows the transition from ZVS operation to hard switching operation. It can be seen that whereas ZVS operation is achieved at the beginning, after a couple periods, the ZVS is lost and hard switching begins. The current level is about 15 A, which corresponds to 0.3 gain. The switching loss characteristics of the system is different before and after this boundary. This proves the analysis.

The variation of the switching frequency and phase-shift angle values versus inverter current is shown in Fig. 15. The switching frequency value is calculated by using optimal trajectory to minimize the losses and improve the efficiency. As a results, the phase-shift and switching frequency values are continuously controlled to track the reference signal and to extend the ZVS operation range and improve the system efficiency. The efficiency of the converter is also investigated. Fig. 16 shows the system efficiency curve obtained from theoretical calculations for different output power levels. The measured maximum efficiency is obtained as 97.4% from simulation and 97.2% from experimental studies. In the battery charger application using a lookup-table-based optimal phase-shift and frequency detection method by only considering power converter, 91% efficiency is obtained [25]. Although it is working at wider output voltage and current ranges, the proposed system provides higher efficiency. In addition, the proposed control scheme with the proposed optimization approach is compared with some other possible control approaches. In Fig. 17, losses of the unfolder inverter, HF transformer, and LLC resonant converter obtained from multiphysics software are given for four control approaches. In the first and second approaches, the switching frequency is kept constant at 30 and 60 kHz, respectively. In third one, the switching frequency is sinusoidally modulated with the sinusoidal current reference. While, the switching frequency is minimum at the zero crossings of the reference current, it is at its maximum value at the peak value of the reference current. The forth one is the proposed method, and the switching frequency is calculated by using the optimal trajectory. As it can be seen from the figure, the proposed approach provides lower losses for the HF transformer and the *LLC* resonant converter, and thus, a higher efficiency can be obtained. The loss of the unfolder inverter is almost same for all four approaches.

The proposed approach is composed of three single-phase units as depicted in Fig. 2. Therefore, for instance, for a 1-MW power level, each unit should be at 1/3-MW power. As it is known, high-frequency SiC devices have higher switching frequencies. Their current/voltage level are quite high and continues to increase. Today, since the primary-side voltage level is at low-voltage level, SiC full modules (e.g., Mitsubishi FMF800DX series), capable to reach this power level, are available in the market [41]. On the other hand, the leakage inductor of the transformer is used as a resonant inductor of the *LLC* converter, thus an external inductor is not used. Therefore, the same path can be followed in a high-power design. In terms of transformer cores, amorphous or nanocrystalline cores can be used at relatively low frequencies. In addition, ferrite cores are also sufficient to reach the mentioned power level with higher

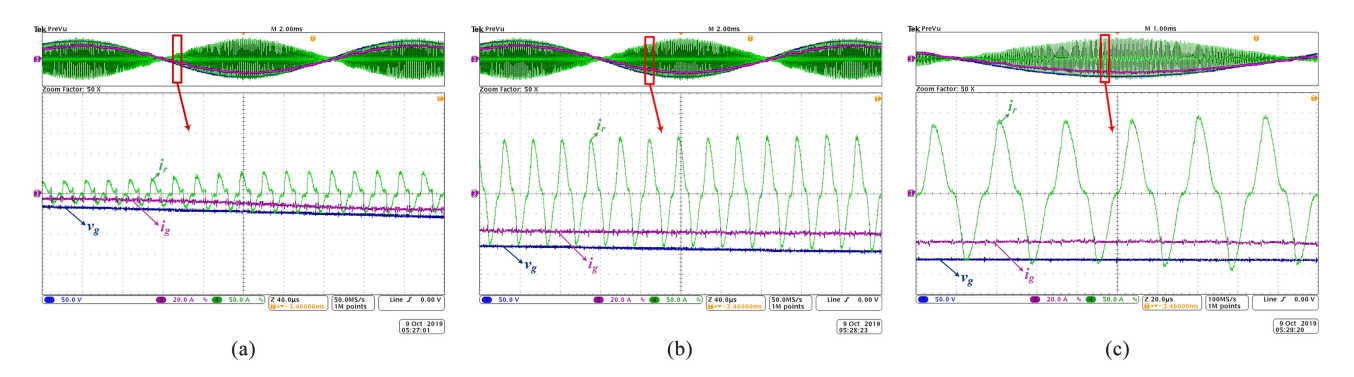


Fig. 12. Resonant network voltage and current waveforms for different phase-shift angles (CH1  $(v_g)$ : 50 V/div, CH3  $(i_g)$ : 20 A/div, and CH4  $(i_r)$ : 50 A/div).

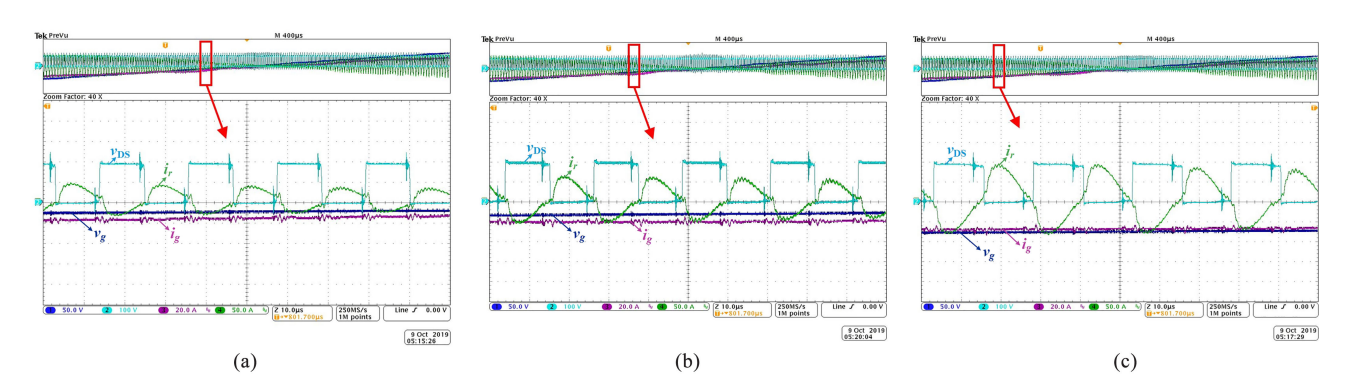


Fig. 13. Grid voltage  $(v_g)$ , the drain–source voltage  $(v_{DS})$  of the T3 (Leg-B upper switch), the grid current, and the resonant tank current waveforms at different instants, (CH1  $(v_g)$ : 50 V/div, CH2  $(v_{DS})$ : 100 V/div, CH3  $(i_g)$ : 20 A/div, and CH4  $(i_r)$ : 50 A/div).

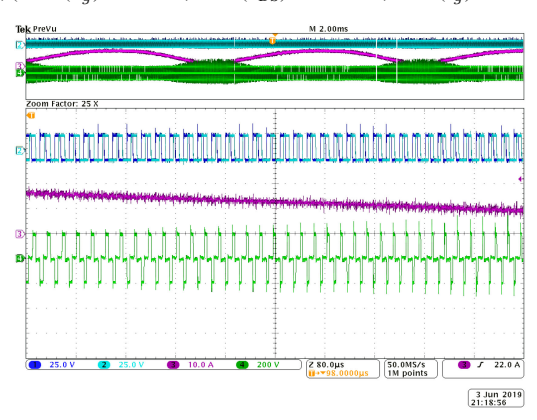
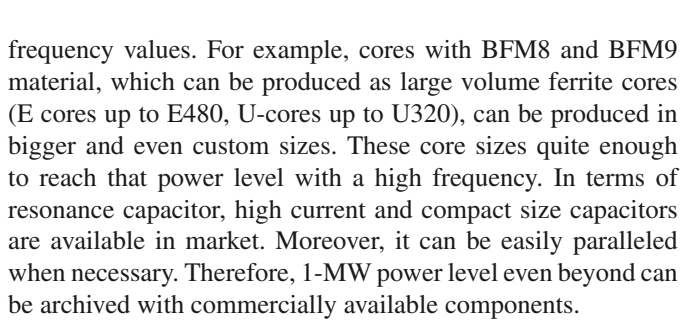


Fig. 14. Resonant network voltage and current waveforms around the ZVS boundary (CH1  $(G_1)$ : 10 V/div, CH2  $(G_3)$ : 10 V/div, CH3  $(i_r)$ : 50 A/div, CH4:  $(v_{\rm inv})$  200 V/div).



Furthermore, the commercially available PV inverters with LFTs are searched to compare with the proposed system. It is seen that the proposed system provides about 19X reduction

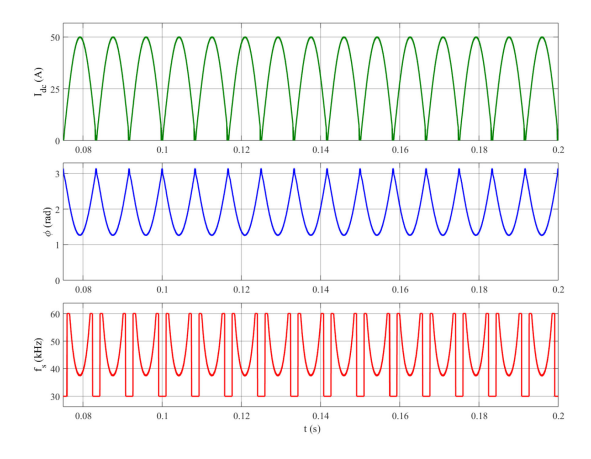


Fig. 15. DC current, phase-shift angle, and switching frequency waveforms obtained from simulation studies.

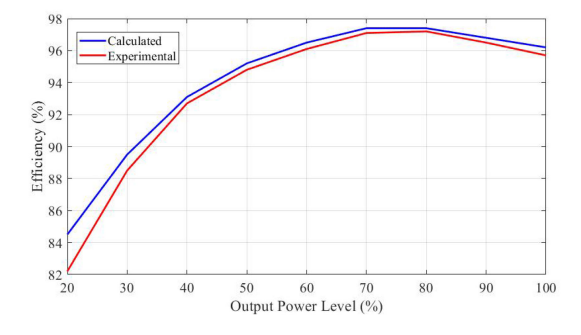


Fig. 16. Calculated and experimental converter efficiency for different power levels.

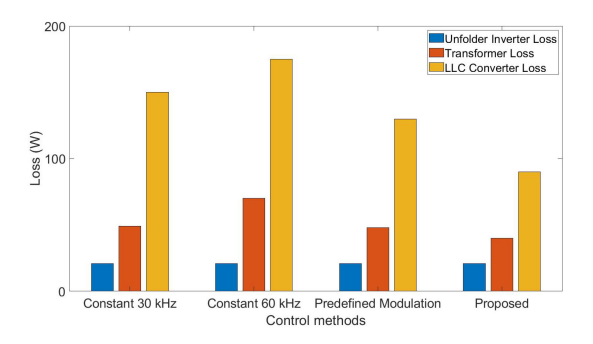


Fig. 17. Losses of the system with different control methods.

in volume and weight. Since the proposed system replaces the LFT in the conventional designs with the HF one, it provides an important reduction in size and volume. The peak efficiency of the commercially available products is in 94%–97.5% range. Although, the peak efficiency values are close to each other, proposed system's efficiency at low load conditions is better than the existing technologies because of the reduced core size and core losses. In addition, at megawatt scale, the LFTs are generally connected to the grid even at night when the PV system is not working, and this causes additional power losses. In the proposed system, since the transformer is the part of the power converter, the transformer does not stay connected to the grid when the system is not running, and thus, this power loss is removed. Since the general control approach is very similar to the conventional grid-connected inverters, the proposed system can provide these advantages without any additional computational burden.

# VI. CONCLUSION

In this study, an *LLC* resonant-controller-based inverter topology is used to regulate the sinusoidal output current of the grid-connected inverter. The ZVS analysis for the general *LLC* converter is presented and limitations about the proposed operation mode is explained. Furthermore, since the traditional frequency control method is not suitable for generating rectified sine wave current signals at grid frequency, the phase-shift angle control method is adopted. The ZVS analysis for the phase-shift control is presented and relation between the ZVS boundary, the phase-shift angle, and the switching frequency is explained. A PI controller is employed to control the converter output current and calculate the phase-shift value. Besides, a Lagrange multiplier method is used to determine the optimal trajectory to define the optimum switching frequency values according to the phase-shift angle to obtain a higher efficiency. It is seen from both simulation and experimental results that the proposed system successfully generates rectified sine wave currents at the dc bus and injects sinusoidal currents to the grid. The high quality waveforms with less harmonic components is obtained. The THD level of the current injected to the grid is measured as 2.62%. It is shown that the proposed control system employing phase-shift control and frequency control schemes provide a fast response and good dynamic behavior. It is also seen that the ZVS operation range is extended and efficiency is improved by both proper transformer design and optimal controlled switching

frequency. Thus, the maximum efficiency of the system is obtained as 97.2%.

## ACKNOWLEDGMENT

Any opinions, findings, and conclusions or recommendations expressed in this material are those of the author(s) and do not necessarily reflect the views of the National Science Foundation.

## REFERENCES

- [1] N. Altin, S. Ozdemir, H. Komurcugil, and I. Sefa, "Sliding-mode control in natural frame with reduced number of sensors for three-phase gridtied LCL-interfaced inverters," *IEEE Trans. Ind. Electron.*, vol. 66, no. 4, pp. 2903–2913, Apr. 2019.
- [2] X. Li and A. K. S. Bhat, "A comparison study of high-frequency isolated DC/AC converter employing an unfolding LCI for grid-connected alternative energy applications," *IEEE Trans. Power Electron.*, vol. 29, no. 8, pp. 3930–3941, Aug. 2014.
- [3] Q. Zhu, L. Wang, A. Q. Huang, K. Booth, and L. Zhang, "7.2-kV single-stage solid-state transformer based on the current-fed series resonant converter and 15-kV SiC MOSFETs," *IEEE Trans. Power Electron.*, vol. 34, no. 2, pp. 1099–1112, Feb. 2019.
- [4] R. Raju, M. Dame, and R. Steigerwald, "Solid-state transformers using silicon carbide-based modular building blocks," in *Proc. IEEE 12th Int.* Conf. Power Electron. Drive Syst., 2017, pp. 1–7.
- [5] N. Altin, S. Ozdemir, and A. Nasiri, "A novel solar PV inverter topology based on an LLC resonant converter," in *Proc. IEEE Energy Convers. Congress Expo.*, Sep. 2019, pp. 6734–6740.
- [6] Y. Shi, R. Li, Y. Xue, and H. Li, "High-frequency-link-based grid-tied PV system with small DC-link capacitor and low-frequency ripple-free maximum power point tracking," *IEEE Trans. Power. Electron.*, vol. 31, no. 1, pp. 328–339, Jan. 2016.
- [7] B. Zhao, Q. Song, W. Liu, and Y. Sun, "Overview of dual-active-bridge isolated bidirectional DC–DC converter for high-frequency-link power-conversion system," *IEEE Trans. Power Electron.*, vol. 29, no. 8, pp. 4091–4106, Aug. 2014.
- [8] J. Zhang, J. Liu, J. Yang, N. Zhao, Y. Wang, and T. Q. Zheng, "An LLC-LC type bidirectional control strategy for an LLC resonant converter in power electronic traction transformer," *IEEE Trans. Ind. Electron.*, vol. 65, no. 11, pp. 8595–8604, Nov. 2018.
- [9] Y. Cho, W. Cha, J. Kwon, and B. Kwon, "High-efficiency bidirectional dab inverter using a novel hybrid modulation for stand-alone power generating system with low input voltage," *IEEE Trans. Power Electron.*, vol. 31, no. 6, pp. 4138–4147, Jun. 2016.
- [10] Y. Wei, Q. Luo, X. Du, N. Altin, A. Nasiri, and J. M. Alonso, "A dual half-bridge LLC resonant converter with magnetic control for battery charger application," *IEEE Trans. Power Electron.*, vol. 35, no. 2, pp. 2196–2207, Feb. 2020.
- [11] L. Chen, A. Amirahmadi, Q. Zhang, N. Kutkut, and I. Batarseh, "Design and implementation of three-phase two-stage grid-connected module integrated converter," *IEEE Trans. Power Electron.*, vol. 29, no. 8, pp. 3881–3892, Aug. 2014.
- [12] A. Karafil, H. Ozbay, and S. Oncu, "Design and analysis of single-phase grid-tied inverter with PDM MPPT-controlled converter," *IEEE Trans. Power Electron.*, vol. 35, no. 5, pp. 4756–4766, May 2020.
- [13] Y. Wei, N. Altin, Q. Luo, and A. Nasiri, "A high efficiency, decoupled on-board battery charger with magnetic control," in *Proc. 7th Int. Conf. Renewable Energy Res. Appl.*, Oct. 2018, pp. 920–925.
- [14] M. F. Menke, A. R. Seidel, and R. V. Tambara, "LLC LED driver small-signal modeling and digital control design for active ripple compensation," *IEEE Trans. Ind. Electron.*, vol. 66, no. 1, pp. 387–396, Jan. 2019.
- [15] D. Yang, C. Chen, S. Duan, J. Cai, and L. Xiao, "A variable duty cycle soft startup strategy for LLC series resonant converter based on optimal current-limiting curve," *IEEE Trans. Power. Electron.*, vol. 31, no. 11, pp. 7996–8006, Nov. 2016.
- [16] J.-H. Jung, H.-S. Kim, M.-H. Ryu, and J.-W. Baek, "Design methodology of bidirectional CLLC resonant converter for high-frequency isolation of DC distribution systems," *IEEE Trans. Power. Electron.*, vol. 28, no. 4, pp. 1741–1755, Apr. 2013.
- [17] S. Chudjuarjeen, A. Sangswang, and C. Koompai, "An improved LLC resonant inverter for induction-heating applications with asymmetrical control," *IEEE Trans. Ind. Electron.*, vol. 58, no. 7, pp. 2915–2925, Jul. 2011.

- [18] N. Shafiei, M. Ordonez, M. Craciun, C. Botting, and M. Edington, "Burst mode elimination in high-power LLC resonant battery charger for electric vehicles," *IEEE Trans. Power. Electron.*, vol. 31, no. 2, pp. 1173–1188, Feb. 2016.
- [19] H. Wu, X. Zhan, and Y. Xing, "Interleaved LLC resonant converter with hybrid rectifier and variable-frequency plus phase-shift control for wide output voltage range applications," *IEEE Trans. Power Electron.*, vol. 32, no. 6, pp. 4246–4257, Jun. 2017.
- [20] Z. Yang, J. Wang, H. Ma, and J. Du, "A wide output voltage LLC series resonant converter with hybrid mode control method," in *Proc. IEEE 2nd Int. Future Energy Electron. Conf.*, 2015, pp. 1–5.
- [21] J. Kim, C. Kim, J. Kim, J. Lee, and G. Moon, "Analysis on load-adaptive phase-shift control for high efficiency full-bridge LLC resonant converter under light-load conditions," *IEEE Trans. Power Electron.*, vol. 31, no. 7, pp. 4942–4955, Jul. 2016.
- [22] M. Xingkui, H. Qisheng, K. Qingbo, X. Yudi, Z. Zhe, and M. A. E. Andersen, "Grid-connected photovoltaic micro-inverter with new hybrid control LLC resonant converter," in *Proc. 42nd Annu. Conf. IEEE Ind. Electron. Soc.*, 2016, pp. 2319–2324.
- [23] M. Rashidi et al., "Design and implementation of a LLC resonant solid state transformer," *IEEE Trans. Ind. Appl.*, vol. 56, no. 4, pp. 3855–3864, Jul./Aug. 2020.
- [24] C. Yeh, C. Chen, M. Lee, and J. Lai, "A hybrid modulation method for single-stage soft-switching inverter based on series resonant converter," *IEEE Trans. Power Electron.*, vol. 35, no. 6, pp. 5785–5796, Jun. 2020.
- [25] S. Liu and F. Zhang, "State variable derivation with numerical approach and efficiency optimisation method for phase-shift LLC converters under wide voltage-gain range," *IET Power Electron.*, vol. 12, no. 7, pp. 1752–1762, Jun. 2019.
- [26] J. Deng, S. Li, S. Hu, C. C. Mi, and R. Ma, "Design methodology of LLC resonant converters for electric vehicle battery chargers," *IEEE Trans. Veh. Technol.*, vol. 63, no. 4, pp. 1581–1592, May 2014.
- [27] H. Wang, S. Dusmez, and A. Khaligh, "Design and analysis of a full-bridge LLC-based PEV charger optimized for wide battery voltage range," *IEEE Trans. Veh. Technol.*, vol. 63, no. 4, pp. 1603–1613, May 2014.
- [28] C. Fei, Y. Yang, Q. Li, and F. C. Lee, "Shielding technique for planar matrix transformers to suppress common-mode EMI noise and improve efficiency," *IEEE Trans. Ind. Electron.*, vol. 65, no. 2, pp. 1263–1272, Feb. 2018.
- [29] C. Fei, F. C. Lee, and Q. Li, "High-efficiency high-power-density LLC converter with an integrated planar matrix transformer for high-output current applications," *IEEE Trans. Ind. Electron.*, vol. 64, no. 11, pp. 9072–9082, Nov. 2017.
- [30] R. Yu, G. K. Y. Ho, B. M. H. Pong, B. W. Ling, and J. Lam, "Computer-aided design and optimization of high-efficiency LLC series resonant converter," *IEEE Trans. Power Electron.*, vol. 27, no. 7, pp. 3243–3256, Jul 2012
- [31] C. Liu, H. Liu, G. Cai, S. Cui, H. Liu, and H. Yao, "Novel hybrid LLC resonant and dab linear DCDC converter: Average model and experimental verification," *IEEE Trans. Ind. Electron.*, vol. 64, no. 9, pp. 6970–6978, Sep. 2017.
- [32] H.-N. Vu and W. Choi, "A novel dual full-bridge LLC resonant converter for CC and CV charges of batteries for electric vehicles," *IEEE Trans. Ind. Electron.*, vol. 65, no. 3, pp. 2212–2225, Mar. 2018.
- [33] H.-P. Park and J.-H. Jung, "PWM and PFM hybrid control method for LLC resonant converters in high switching frequency operation," *IEEE Trans. Ind. Electron.*, vol. 64, no. 1, pp. 253–263, Jan. 2017.
- [34] U. Kundu and P. Sensarma, "A unified approach for automatic resonant frequency tracking in LLC DCDC converter," *IEEE Trans. Ind. Electron.*, vol. 64, no. 12, pp. 9311–9321, Dec. 2017.
- [35] R. Ren, B. Liu, E. A. Jones, F. Wang, Z. Zhang, and D. Costinett, "Accurate ZVS boundary in high switching frequency LLC converter," in *Proc. IEEE Energy Convers. Congr. Expo.*, Sep. 2016, pp. 1–6.
- [36] S. M. S. I. Shakib and S. Mekhilef, "A frequency adaptive phase shift modulation control based LLC series resonant converter for wide input voltage applications," *IEEE Trans. Power. Electron.*, vol. 32, no. 11, pp. 8360–8370, Nov. 2017.
- [37] A. E. Shafei, S. Ozdemir, N. Altin, G. Jean-Pierre, and A. Nasiri, "A high power high frequency transformer design for solid state transformer applications," in *Proc. 8th Int. Conf. Renewable Energy Res. Appl.*, Nov. 2019, pp. 904–909.
- [38] S. Balci, I. Sefa, and N. Altin, "Design and analysis of a 35 kVA medium frequency power transformer with the nanocrystalline core material," *Int. J. Hydrogen Energy*, vol. 42, no. 28, pp. 17895–17909, Jul. 2017.

- [39] J. Liu, J. Mookken, and K. L. Wong, "Highly efficient, and compact ZVS resonant full bridge converter using 1200V SiC MOSFETs," in *Proc. PCIM Europe Int. Exhib. Conf. Power Electron, Intell. Motion, Renewable Energy Energy Manage.*, May 2014, pp. 1–8.
- [40] Y. Tang, W. Ding, and A. Khaligh, "A bridgeless totem-pole interleaved PFC converter for plug-in electric vehicles," in *Proc. IEEE Appl. Power Electron. Conf. Expo.*, Mar. 2016, pp. 440–445.
- [41] E. Wiesner, K. Masuda, and M. Joko, "New 1200V full SiC module with 800a rated current," in *Proc. 17th Eur. Conf. Power Electron. Appl.*, 2015, pp. 1–9.



**Necmi Altin** (Senior Member, IEEE) received the B.Sc., M.Sc., and Ph.D. degrees in electrical engineering from Gazi University, Ankara, Turkey, in 2000, 2003, and 2009, respectively.

He joined the Department of Electrical and Electronics Engineering, Faculty of Technology, Gazi University as an Assistant Professor in 2010, and was promoted to a Full Professor position in 2020. He has been a Visiting Scholar with the University of Wisconsin-Milwaukee, Milwaukee, WI, USA, from 2017 to 2019. His current research interests include

power electronics, grid interactive inverters, and control systems. He has authored and coauthored more than 150 journal and conference papers, and a book chapter.



**Saban Ozdemir** (Senior Member, IEEE) received the B.Sc., M.Sc., and Ph.D. degrees in electrical education from Gazi University, Ankara, Turkey, in 2004, 2007, and 2013, respectively.

From 2008 to 2009, he was with Baskent University, Ankara. In 2009, he joined Gazi University. He is currently an Associate Professor with the Department of Electrical and Electronics Engineering, Faculty of Technology, Gazi University. From 2017 to 2018, he was a Visiting Scholar, and from 2018 to 2019, he was a Research Associate with the University of

Wisconsin-Milwaukee, Milwaukee, WI, USA. His current research interests include power electronics, solid-state transformers, and resonant converter.



Mehdy Khayamy (Member, IEEE) received the B.Sc. degree in electrical engineering from Chamran University, Ahvaz, Iran, in 2004, M.Sc. degree in electrical engineering from the University of Tehran, Iran, in 2008, and the Ph.D. degree in electrical engineering from Tennessee Technological University, Cookville, TN, USA, in 2017.

After his M.S., he worked as the Test and Commissioning Engineer for the generator field rectifier, static excitation system, and generator/turbine initial start-up, static frequency converter. After his Ph.D.,

he worked as a Postdoc with UWM, an RD engineer with Eaton, and currently a Control Engineer with Motiv PS, Hayward, CA, USA. His research interests include the development of a control algorithm for power electronic converters.



**Adel Nasiri** (Fellow IEEE) received the B.S. and M.S. degrees in electrical engineering from the Sharif University of Technology, Tehran, Iran, in 1996 and 1998, respectively, and the Ph.D. degree in electrical engineering from the Illinois Institute of Technology, Chicago, IL, USA, in 2004.

He is currently a Distinguished Professor with the Electrical Engineering Department, University of South Carolina, Columbia, SC, USA. His research interests include smart and connected energy systems, energy storage, and microgrids. Previously, he

worked with the University of Wisconsin-Milwaukee from 2005 to 2021 and served in various roles. He has authored and coauthored many technical journal and conference papers and coauthored two books on related topics. He also holds seven patent disclosures.